Chapter 29

Fluid-Driven Fracture in a Poroelastic Rock

Yevhen Kovalyshen and Emmanuel Detournay

Additional information is available at the end of the chapter

http://dx.doi.org/10.5772/56460

1. Introduction

Hydraulic fracturing is commonplace in the geo-industry, whether designed or unintended; e.g., stimulation of hydrocarbons reservoirs [1, 2], disposal of waste water [3], waterflooding operations [4], enhanced oil recovery by injection of CO2 [5], and preconditioning of rock mass in the mining industry [6, 7]. Nonetheless, modeling of hydraulic fracturing usually relies on oversimplified assumptions [1, 8]; in particular, fluid leak-off is often studied within Carter's model [9] that assumes that the transport of the filtrate and the porous fluid through the porous medium is one-dimensional. While this assumption is quite reasonable in the case of short treatments such as hydraulic fracturing of a hydrocarbons reservoir [2], it is unlikely to be applicable for injection operations over long periods of time.

This study is part of an ongoing effort to rigorously introduce large-scale 3D diffusion in a model of hydraulic fracture. The increase of pore pressure around the fracture caused by fluid leak-off from the fracture leads to an expansion of the porous medium. This expansion can be accounted for by the introduction of the so-called backstress [10, 11]. By definition, the backstress would be the stress induced across the fracture plane if the fracture were closed. Here we restrict our investigation to the toughness-dominated regime of propagation, for which the viscosity of the fluid is negligible. In other words we assume that the energy spent for hydraulic fracturing is mainly due to the rock damage rather than due to dissipation associated with viscous flow of the fracturing fluid. Setting the fracturing fluid viscosity to be equal to zero implies that the fluid pressure inside the fracture is uniform.

Previous works on the toughness-dominated regimes with leak-off include a detailed examination of the case of the Carter's leak-off model by means of scaling and asymptotic analyses [12] and an analysis of a "stationary" 3D leak-off under conditions of very slow fracture propagation, when the pore pressure around the fracture is always in equilibrium [13]. A model for the plane strain propagation of a natural fracture through a porous medium was proposed by [14], who introduced an efficient approach to calculate of the fluid exchange

volume between the fracture and the medium. This approach relies on decomposing the evolving pressure loading inside the growing fracture into a series of pressure impulses and then on representing the actual fluid exchange volume by the superposition of fluid exchanges induced by a single impulse [11]. Despite algebraic errors in the main expression for the fluid exchange volume (equation (7) of [14]), the idea introduced by these authors is at the core of the approach summarized in this paper and described in more details in [15].

In this paper we build a general model of a penny-shaped hydraulic fracture driven by a zero viscosity fluid through a poroelastic medium. The model accounts for the backstress effect, which was not considered in earlier efforts [12–14]. This work makes use of the response of a poroelastic medium to an impulse of pore pressure applied to a penny-shaped domain; namely, $u(r,t)$, the component of the fluid displacement, normal to the disc, and $S_b(r,t)$, the normal stress component [15]. The main restrictive assumptions of this analysis is the absence of a low permeability cake build-up and the neglect of the poroelastic solid-to-fluid coupling. The later assumption was studied by [11], who have concluded that in the case of hydraulic boundary conditions when the pore pressure is prescribed, the fluid exchange between the fracture and the medium calculated via poroelastic theory is nearly identical to that computed by uncoupled diffusion equation. Throughout this work we intensively use scaling and asymptotic analyses; in particular, we show that the parametric space is a prism. In this parametric space, the case of the Carter's leak-off model [12] occupies one edge of this prism, whereas the pseudo steady-state model [13] covers one face.

The main objective of the analysis is to solve for the evolution of the fracture radius $R(t)$, the fracturing fluid pressure $p_{\text{in}}(t)$, and the efficiency of the hydraulic fracturing $\mathcal{E}(t) \equiv V_{\text{crack}}/V_{\text{inject}}$, where V_{crack} is the volume of the fracture and V_{inject} is the volume of the injected fracturing fluid.

2. Mathematical model

2.1. Problem definition

We consider a penny-shaped fracture driven by injection of an incompressible fluid, at a constant rate Q_0 (see Fig.1). The crack propagates through an infinite, homogeneous, brittle, poroelastic rock saturated by a fluid which has the same physical properties as the filtrate, i.e., these fluids are physically indistinguishable inside the porous medium. The medium is characterized by Young's modulus E, Poisson's ratio ν, fracture toughness K_{Ic}, intrinsic permeability κ, storage coefficient S, Biot coefficient α. Prior to the injection of fluid, the pore pressure field p_0 is uniform. Also there exists a far-field compressive stress σ_0, perpendicular to the fracture plane.

2.2. Dimensional formulation

We start from the global fluid balance equation

$$V_{\text{inject}}(t) = V_{\text{crack}}(t) + V_{\text{leak}}(t). \tag{1}$$

http://dx.doi.org/10.5772/56460

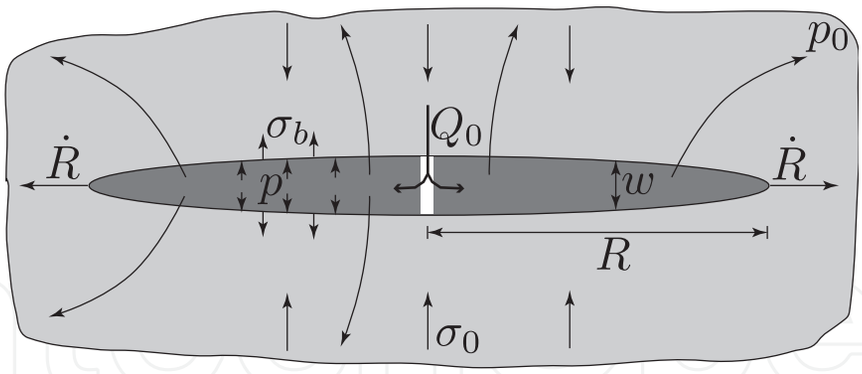

Figure 1. sketch of the problem

The quantity $V_{\text{inject}}(t) = Q_0 t$ denotes the volume of injected fracturing fluid, while $V_{\text{crack}}(t)$ is the fracture volume

$$V_{\text{crack}}(t) = 2\pi R^2(t) \int_0^1 w[R(t)s, t]\, sds. \tag{2}$$

In the above $R(t)$ is the fracture radius, and $w(r,t)$ is the fracture opening.

The elasticity integral equation [16, 17]

$$w(r,t) = \frac{8}{\pi}\frac{R}{E'} \int_0^1 \{p(t) + \sigma_b[R(t)s, t] - \sigma_0\}\, G\left[\frac{r}{R(t)}, s\right] sds, \tag{3}$$

links the fracture aperture $w(r,t)$ to the fracturing fluid pressure $p(t)$ and the backstress, $\sigma_b(r,t)$. In (3), $E' \equiv E/(1-\nu^2)$ denotes the plane strain modulus. The elasticity kernel $G(\xi, s)$ is given by

$$G(\xi, s) = \begin{cases} \frac{1}{\xi} F\left(\arcsin\sqrt{\frac{1-\xi^2}{1-s^2}}, \frac{s^2}{\xi^2}\right), & \xi > s \\ \frac{1}{s} F\left(\arcsin\sqrt{\frac{1-s^2}{1-\xi^2}}, \frac{\xi^2}{s^2}\right), & \xi < s \end{cases}, \tag{4}$$

with $F(\phi, m)$ denoting the incomplete elliptic integral of the first kind [18].

Substitution of the elasticity equation (3) into (2) yields

$$V_{\text{crack}}(t) = \frac{16}{3}\frac{R^3(t)}{E'} \left\{p(t) - \sigma_0 + 3\int_0^1 \sigma_b[R(t)s, t]\sqrt{1-s^2}\, sds\right\}. \tag{5}$$

As indicated earlier, we can represent the continuous evolution of the fluid pressure inside the crack by a sum of spatially uniform time impulses of pressure. Then, the leaked-off volume V_{leak} and the backstress σ_b can be written as

$$V_{\text{leak}}(t) = \int_0^t U[R(s), t-s]\,[p(s) - p_0]\, ds, \tag{6}$$

$$\sigma_b(r,t) = \int_0^t S_b[R(s), r, t-s]\,[p(s) - p_0]\,ds, \tag{7}$$

where $U(R,t)$ is the volume of the fracturing fluid that has escaped from a fracture of radius R at an elapsed time t after a uniform unit impulse of pressure has been applied, and $S_b(R,r,t)$ is the generated backstress. In the following we refer to $U(R,t)$ as the leak-off Green function, and to $S_b(R,r,t)$ as the backstress Green function.

Simple scaling analysis reveals the following relations between these dimensional Green functions $U(R,t)$, $S_b(R,r,t)$ and the dimensionless ones $\Psi(\tau)$, $\Xi(\xi,\tau)$ [15]

$$U(R,t) = \frac{SR^3}{T_R}\Psi\left(\frac{t}{T_R}\right), \quad S_b(R,r,t) = \frac{\eta}{T_R}\Xi\left(\frac{r}{R}, \frac{t}{T_R}\right), \quad T_R = \frac{R^2}{4c}, \tag{8}$$

where $c = \kappa/S$ is the diffusion coefficient, $\eta = \alpha(1-2\nu)/2(1-\nu)$ is the poroelastic stress coefficient.

We close the formulation of the problem with the propagation criterion

$$K_{Ic} = \frac{2}{\sqrt{\pi}}R^{1/2}(t)\int_0^1 \frac{p[sR(t),t] + \sigma_b[sR(t),t] - \sigma_0}{\sqrt{1-s^2}}sds, \tag{9}$$

The model has thus only two unknowns: the fracturing fluid pressure $p(t)$ and the fracture radius $R(t)$.

2.3. Dimensionless formulation

The problem depends on seven dimensional parameters: K_{Ic}, E', Q_0, c, S, σ_0, and p_0, and one dimensionless parameter η. It is possible to reduce this set of parameters to five dimensionless quantities. Inspired by earlier works on hydraulic fracture [19], we introduce the scaling

$$r = R(t)\,\xi, \quad R(t) = L(t)\,\rho(t),$$

$$p(t) - \sigma_0 = \frac{K_{Ic}}{L^{1/2}(t)}\Pi(t), \quad \sigma_b(r,t) = \frac{K_{Ic}}{L^{1/2}(t)}\Sigma(\xi,t). \tag{10}$$

where $\rho(t) \sim 1$ is the dimensionless radius, $\Pi(t) \sim 1$ is the dimensionless net pressure, $\Sigma(\xi,t)$ is the dimensionless back stress, and $L(t) \sim R(t)$ is the characteristic size of the fracture. This scaling is thus time-dependent. Moreover we have not yet defined the parameter $L(t)$. Below we show that the parameter $L(t)$ can be defined for different propagation regimes in such a way that the dimensionless quantities ρ, Π, and Σ do not depend on time.

In the scaling (10) the governing equations transform as follows.

http://dx.doi.org/10.5772/56460

- Backstress equation (7) after substitution of (8)

$$\Sigma(\xi,t)=4\eta\mathcal{G}_d(t)\int_0^1\frac{L^2(t)}{L^2(ts)}\frac{1}{\rho^2(ts)}\Xi\left[\xi\frac{L(t)\rho(t)}{L(ts)\rho(ts)},4\mathcal{G}_d(t)\frac{L^2(t)}{L^2(ts)}\frac{1-s}{\rho^2(ts)}\right]\times$$

$$\times\left[\mathcal{G}_\sigma(t)+\sqrt{\frac{L(t)}{L(ts)}}\Pi(ts)\right]ds, \tag{11}$$

- Propagation criterion (9) combined with (11)

$$1=\frac{2}{\sqrt{\pi}}\rho^{1/2}(t)\,\Pi(t)+K_{bs}(t), \tag{12}$$

- Volume balance equation (1), where we substituted (5), (6), (8), and (12)

$$1=\frac{8\sqrt{\pi}}{3}\mathcal{G}_v(t)\,\rho^{5/2}(t)\,[1+V_{bs}(t)-K_{bs}(t)]+$$

$$+4\mathcal{G}_c(t)\int_0^1\frac{L(ts)}{L(t)}\rho(ts)\,\Psi\left[4\mathcal{G}_d(t)\frac{L^2(t)}{L^2(ts)}\frac{1-s}{\rho^2(ts)}\right]\left[\mathcal{G}_\sigma(t)+\sqrt{\frac{L(t)}{L(ts)}}\Pi(ts)\right]ds. \tag{13}$$

Here $K_{bs}(t)$ is the change of the stress intensity factor due to the backstress

$$K_{bs}(t)=\frac{4\eta\mathcal{G}_d(t)}{\rho^{1/2}(t)}\int_0^1\frac{L(t)}{L(ts)}\frac{1}{\rho(ts)}k_{bs}\left[\frac{L(t)\rho(t)}{L(ts)\rho(ts)},4\mathcal{G}_d(t)\frac{L^2(t)}{L^2(ts)}\frac{1-s}{\rho^2(ts)}\right]\times$$

$$\left[\mathcal{G}_\sigma(t)+\sqrt{\frac{L(t)}{L(ts)}}\Pi(ts)\right]ds, \tag{14}$$

and $V_{bs}(t)$ is the change of the fracture volume due to the backstress

$$V_{bs}(t)=\frac{4\eta\mathcal{G}_d(t)}{\rho^{5/2}(t)}\int_0^1\rho(ts)\frac{L(ts)}{L(t)}v_{bs}\left[\frac{L(t)\rho(t)}{L(ts)\rho(ts)},4\mathcal{G}_d(t)\frac{L^2(t)}{L^2(ts)}\frac{1-s}{\rho^2(ts)}\right]\times$$

$$\left[\mathcal{G}_\sigma(t)+\sqrt{\frac{L(t)}{L(ts)}}\Pi(ts)\right]ds, \tag{15}$$

where

$$k_{bs}(\mathcal{R},\tau)=\frac{2}{\sqrt{\pi}}\int_0^{\mathcal{R}}\frac{\xi\Xi(\xi,\tau)}{\sqrt{\mathcal{R}^2-\xi^2}}d\xi, \tag{16}$$

$$v_{bs}(\mathcal{R},\tau)=\frac{6}{\sqrt{\pi}}\int_0^{\mathcal{R}}\xi\sqrt{\mathcal{R}^2-\xi^2}\Xi(\xi,\tau)\,d\xi. \tag{17}$$

The above governing equations thus depend on four time-dependent dimensionless groups:

- Storage group

$$\mathcal{G}_v(t)=\frac{K_{Ic}}{Q_0E'}\frac{L^{5/2}(t)}{t}, \tag{18}$$

  which is proportional to the fraction of the injected fluid volume stored in the fracture;

- Leak-off group

$$\mathcal{G}_c(t)=\frac{cSK_{Ic}}{Q_0}L^{1/2}(t), \tag{19}$$

  which characterizes the amount of the fluid that has leaked into the formation;

- Diffusion group

$$\mathcal{G}_d=\frac{ct}{L^2(t)}, \tag{20}$$

  which is related to the diffusion process with $\sqrt{\mathcal{G}_d}$ proportional to the ratio of the diffusion length scale to the fracture size. Thus this dimensionless group is small, $\mathcal{G}_d \ll 1$, in the case of 1D diffusion and large in the case of 3D diffusion, $\mathcal{G}_d \gg 1$;

- Pressure group

$$\mathcal{G}_\sigma(t)=\frac{\sigma_0-p_0}{K_{Ic}}L^{1/2}(t)\sim\frac{\sigma_0-p_0}{p-\sigma_0}, \tag{21}$$

  which describes the effect of the material toughness on the net fluid pressure $p-\sigma_0$ compared to σ_0-p_0. Indeed, in the case of small toughness when $K_{Ic}\to 0$ and $\mathcal{G}_\sigma\to\infty$, the fracturing fluid pressure p can be assumed to be equal to the confining stress σ_0 from a diffusion point of view, i.e., $p\approx\sigma_0$. Whereas in the case of large toughness when $K_{Ic}\to\infty$ and $\mathcal{G}_\sigma\to 0$, the net fluid pressure $p-\sigma_0$ is large compared to σ_0-p_0.

The only unknown here are the fracture radius $\rho(\tau)$ and fracturing fluid pressure $\Pi(\tau)$.

3. Propagation regimes

The problem under study has six propagation regimes. Therefore it is convenient to represent the fracture propagation by a trajectory line lying inside the prismatic parametric space shown in Fig. 2. The vertices of this prism represent the different propagation regimes; namely,

http://dx.doi.org/10.5772/56460

- the K_0-vertex represents the storage-dominated regime with 1D diffusion, during which most of the injected fluid is stored inside the fracture;
- the $\tilde{K}_{\kappa 0}$-vertex is related to the leak-off-dominated regime with 1D diffusion, when the net fluid pressure $p - \sigma_0$ is large compared to $\sigma_0 - p_0$;
- the $\tilde{K}_{\sigma 0}$-vertex is another leak-off-dominated regime with slow 1D diffusion, where from a diffusion point of view the fracturing fluid pressure p is approximately equal to the confining stress σ_0;
- the K_∞-vertex is the storage-dominated regime with pseudo steady-state 3D diffusion;
- the $\tilde{K}_{\kappa\infty}$-vertex is the pseudo steady-state (3D) diffusion version of the $\tilde{K}_{\kappa 0}$-vertex;
- the $\tilde{K}_{\sigma\infty}$-vertex is the pseudo steady-state (3D) diffusion version of the $\tilde{K}_{\sigma 0}$-vertex.

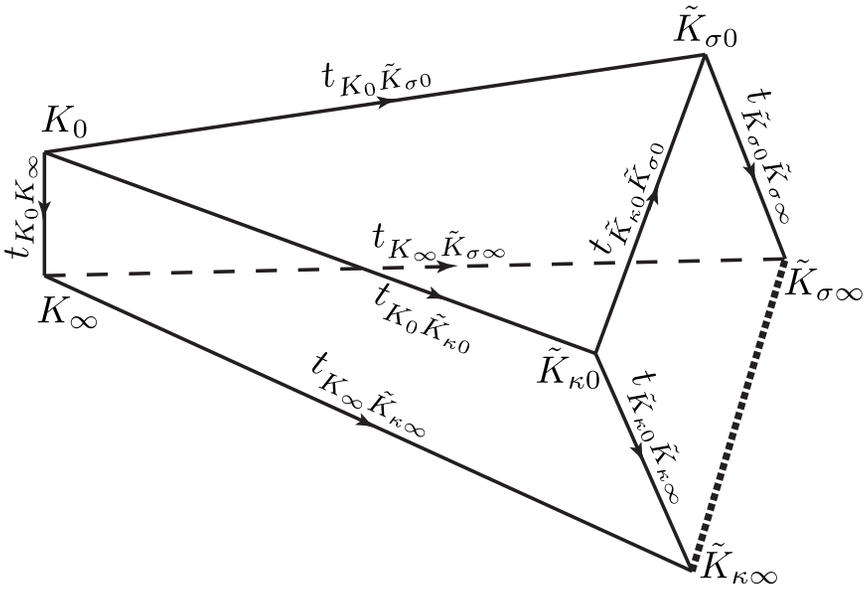

Figure 2. Parametric space

In the transition from one regime to another, the dominance of one physical process is displaced by the dominance of another one. For example the transition $K_\infty\tilde{K}_{\kappa\infty}$ is governed by $\mathcal{G}_c/\mathcal{G}_v$, such that $\mathcal{G}_c/\mathcal{G}_v = 0$ for the K_∞-vertex, and $\mathcal{G}_c/\mathcal{G}_v = \infty$ for the $\tilde{K}_{\kappa\infty}$-vertex. In another example, the transition from 1D to 3D diffusion is governed by $\mathcal{G}_d$, such that $\mathcal{G}_d = 0$ for 1D diffusion, and $\mathcal{G}_d = \infty$ for 3D diffusion.

Usually, each propagation regime is studied in an intrinsic time-dependent scaling, such that the propagation of a fracture in a given propagation regime does not depend on time in this scaling. In other words, each propagation regime is characterized by a self-similar solution. This intrinsic scaling is introduced in such a way that all dimensionless groups corresponding to the dominant physical processes are equal to 1, whereas all the other groups are small compared to 1. These small dimensionless groups are still time-dependent, therefore it is easy to estimate when a given propagation regime is valid. Also using these small time-dependent groups we can easily calculate the characteristic transition times between different propagation regimes. For example, in order to calculate the characteristic transition time t_{AB} between the two propagation regimes A and B, one should follow the following procedure: first, introduce a scaling intrinsic to the propagation regime A; second, obtain in

ver-	definition			scaling		solution
tex	$\mathcal{G}_d$	$\mathcal{G}_\sigma$	$\mathcal{G}_v/\mathcal{G}_c$	definition	$L(t)$	ρ
K_0	$\ll 1$	–	$\gg \mathcal{G}_d^{-1/2}\max[1,\mathcal{G}_\sigma]$	$\mathcal{G}_v = 1$	$\left(\frac{Q_0 E'}{K_{Ic}}t\right)^{2/5}$	$\left(\frac{3}{8\sqrt{\pi}}\right)^{2/5}$
$\tilde{K}_{\kappa 0}$	$\ll 1$	$\ll 1$	$\ll \mathcal{G}_d^{-1/2}$	$\mathcal{G}_c^{(1D)} = 1$	$\left(\frac{Q_0 \mathcal{I}^{-1} t^{1/2}}{c^{1/2} S K_{Ic}}\right)^{2/3}$	$\frac{2^{2/3}}{\pi^{4/3}}$
$\tilde{K}_{\sigma 0}$	$\ll 1$	$\gg 1$	$\ll \mathcal{G}_d^{-1/2}\mathcal{G}_\sigma$	$\mathcal{G}_c^{(1D)}\mathcal{G}_\sigma = 1$	$\left[\frac{Q_0 \mathcal{I}^{-1} t^{1/2}}{c^{1/2} S(\sigma_0 - p_0)}\right]^{1/2}$	$\pi^{-3/4}$
K_∞	$\gg 1$	–	$\gg \max[1,\mathcal{G}_\sigma]$	$\mathcal{G}_v = 1$	$\left(\frac{Q_0 E'}{K_{Ic}}t\right)^{2/5}$	$\left(\frac{3}{8\sqrt{\pi}}\right)^{2/5}$
$\tilde{K}_{\kappa\infty}$	$\gg 1$	$\ll 1$	$\ll 1$	$\mathcal{G}_c = 1$	$\left(\frac{Q_0}{cSK_{Ic}}\right)^2$	$\frac{(1-\eta)^2}{16\pi}$
$\tilde{K}_{\sigma\infty}$	$\gg 1$	$\gg 1$	$\ll \mathcal{G}_\sigma$	$\mathcal{G}_c\mathcal{G}_\sigma = 1$	$\frac{Q_0}{cS(\sigma_0 - p_0)}$	$\frac{1-\eta}{8}$

Here $\mathcal{G}_c^{(1D)} \equiv \frac{\mathcal{G}_c}{\mathcal{G}_d^{1/2}}\left(1 - \frac{4\eta}{E'S}\right)$ and $\mathcal{I} \equiv 1 - \frac{4\eta}{E'S}$

Table 1. Propagation regimes and corresponding scalings

terms of this intrinsic scaling an expression for the dimensionless group $\mathcal{G}_B^{(A)}(t)$, which is dominant in the regime B, whereas it is small in the regime A; and third, solve the equation $\mathcal{G}_B^{(A)}(t_{AB}) = 1$ to obtain the characteristic transition time t_{AB}.

Different scalings can be introduced by defining the length scale $L(t)$, see (21)-(18). We define different propagation regimes in terms of the dimensionless groups (21)-(18) in Table 1, where we also introduce the scalings intrinsic to each of these propagation regimes. The transition times between different propagation regimes are given by

- $K_0 K_\infty$- edge

$$t_{K_0 K_\infty} = \frac{Q_0^4 E'^4}{c^5 K_{Ic}^4};$$

- $K_0 \tilde{K}_{\kappa 0}$- edge

$$t_{K_0 \tilde{K}_{\kappa 0}} = \left[c^{1/2} S \left(\frac{K_{Ic}^2 E'^3}{Q_0^2}\right)^{1/5}\left(1 - \frac{4\eta}{E'S}\right)\right]^{-10};$$

- $K_0 \tilde{K}_{\sigma 0}$- edge

$$t_{K_0 \tilde{K}_{\sigma 0}} = \left[c^{1/2} S(\sigma_0 - p_0)\left(\frac{E'^4}{Q_0 K_{Ic}^4}\right)^{1/5}\left(1 - \frac{4\eta}{E'S}\right)\right]^{-10/3};$$

- $\tilde{K}_{\kappa 0}\tilde{K}_{\sigma 0}$- edge

$$t_{\tilde{K}_{\kappa 0}\tilde{K}_{\sigma 0}} = \left[\frac{c^{1/2} S K_{Ic}^4}{(\sigma_0 - p_0)^3 Q_0}\left(1 - \frac{4\eta}{E'S}\right)\right]^2;$$

http://dx.doi.org/10.5772/56460

- $\tilde{K}_{\kappa 0}\tilde{K}_{\kappa\infty}$- edge

$$t_{\tilde{K}\kappa 0\tilde{K}\kappa\infty} = \frac{Q_0^4}{c^5 S^4 K_{Ic}^4};$$

- $\tilde{K}_{\sigma 0}\tilde{K}_{\sigma\infty}$- edge

$$t_{\tilde{K}\sigma 0\tilde{K}\sigma\infty} = \frac{Q_0^2}{c^3 S^2 \left(\sigma_0 - p_0\right)^2};$$

- $K_\infty\tilde{K}_{\kappa\infty}$- edge

$$t_{K_\infty\tilde{K}\kappa\infty} = \frac{Q_0^4}{c^5 S^5 E' K_{Ic}^4};$$

- $K_\infty\tilde{K}_{\sigma\infty}$- edge

$$t_{K_\infty\tilde{K}\sigma\infty} = \sqrt{\frac{Q_0^3 K_{Ic}^2}{c^5 S^5 E'^2 \left(\sigma_0 - p_0\right)^5}}.$$

- $\tilde{K}_{\kappa\infty}\tilde{K}_{\sigma\infty}$-edge is self-similar, i.e., the transition along this edge is impossible. Moreover all trajectory lines of the fracture propagation begin at the K_0-vertex and end at some point of the $\tilde{K}_{\kappa\infty}\tilde{K}_{\sigma\infty}$-edge.

The case of the Carter's leak-off model studied in [12] corresponds to the $K_0\tilde{K}_{\sigma 0}$-edge, whereas the pseudo steady-state model introduced in [13] corresponds to the $K_\infty\tilde{K}_{\kappa\infty}\tilde{K}_{\sigma\infty}$-face with $\eta = 0$.

Interestingly the fracture radius ρ is the same in the two different storage-dominated regimes K_0 and K_∞ (see Table 1), while the fracturing fluid pressure is different [15]. Therefore the poroelastic effects split the storage dominated regime (denoted previously as the K-vertex [12, 17]) into two sub-regimes: the K_0-vertex (1D diffusion) which is similar to the former K-vertex, and the K_∞-vertex (pseudo steady-state diffusion) characterized by a higher pressure. The essence of the difference between these two regimes is illustrated in Fig. 3. Initially the fracture front propagates faster than the diffusion front, therefore the diffusion length scale is small compared to the size of the fracture and the diffusion is one dimensional. As time goes on, the diffusion front catches up and then passes the fracture front, making the diffusion length scale to be larger than the fracture size, and, as a result, switching the propagation regime from the 1D diffusion to the pseudo steady-state (3D) diffusion.

4. Methodology

Inclusion of diffusion and poroelastic effects into the model of penny-shaped hydraulic fracture model propagation in the toughness-dominated regime thus requires evaluating the convolution type integrals [see (11), (13)-(15)]. Indeed, calculation of the fracturing fluid volume which has leaked into the formation requires a "convolution" on $\Psi(\tau)$ [see (13)], whereas evaluation of the backstress $\Sigma(\xi, t)$ and the related fracture volume $V_{bs}(t)$ and stress intensity factor $K_{bs}(t)$ changes requires "convolutions" on $\Xi(\xi, \tau)$. These "convolutions"

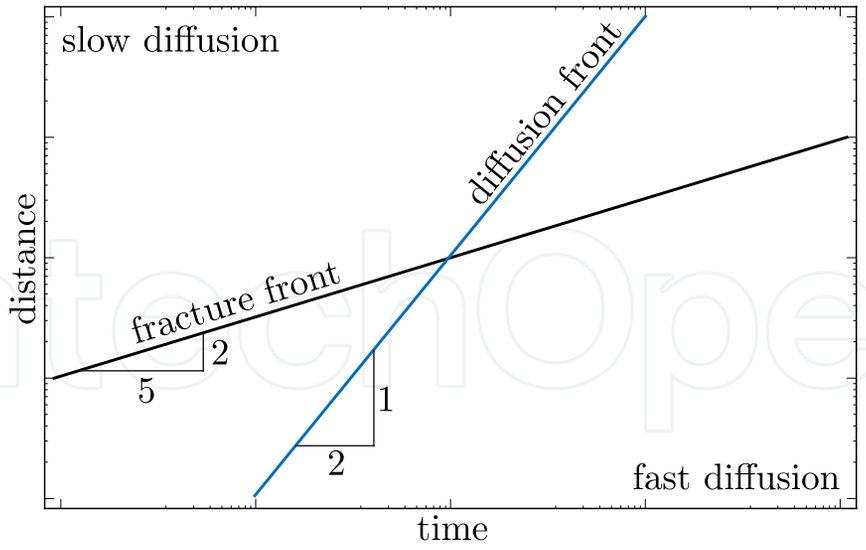

Figure 3. Physical interpretation of the difference between K_0- and K_∞-vertices

involves both arguments of $\Xi(\xi,\tau)$ and are much more complicated than the "convolution" on the single argument $\Psi(\tau)$ [see (11), (14), and (15)].

To simplify the calculations of $V_{bs}(t)$ and $K_{bs}(t)$, we introduce two additional functions $v_{bs}(\mathcal{R},\tau)$ and $k_{bs}(\mathcal{R},\tau)$, such that "convolutions" on these functions yield $V_{bs}(t)$ and $K_{bs}(t)$ [see (14)-(17)]. Physically the function $v_{bs}(\mathcal{R},\tau)$ can be interpreted as the volume change of a fracture of radius $\mathcal{R}>1$ at an elapsed time τ due to the backstress generated by a unit impulse of the pore pressure applied at time $\tau=0$ along the part of the fracture $\mathcal{R}$ located inside the unit circle $\xi<1$. The function $k_{bs}(\mathcal{R},\tau)$ is the corresponding change in the stress intensity factor. Note that there is a simple connection between $k_{bs}(\mathcal{R},\tau)$ and $v_{bs}(\mathcal{R},\tau)$ [see (16), (17)]

$$k_{bs}(\mathcal{R},\tau)=\frac{2}{3}\frac{\partial v_{bs}(\mathcal{R},\tau)}{\partial \mathcal{R}^2}. \tag{22}$$

Small-time asymptotes of $k_{bs}(\mathcal{R},\tau)$ and $v_{bs}(\mathcal{R},\tau)$

The small-time asymptote of $\Xi(\xi,\tau)$ is given by [15]

$$\Xi_0(\xi,\tau)=-\frac{1}{\pi^{3/2}\tau^{1/2}}\left\{(1-\xi)^{-1}E\left[\frac{4\xi}{(1+\xi)^2}\right]+(1+\xi)^{-1}K\left[\frac{4\xi}{(1+\xi)^2}\right]\right\}, \tag{23}$$

where $K(x)$ and $E(x)$ are the complete elliptic integrals of the first and second kinds respectively [18]. This asymptote has a strong singularity $1/(1-\xi)$, which causes significant problems in numerical simulations. Also one can observe a separation of variables, which simplifies the evaluation of $k_{bs}(\mathcal{R},\tau)$ and $v_{bs}(\mathcal{R},\tau)$ at small time.

Substitution of this small-time asymptote $\Xi_0(\xi,\tau)$ into the expression for $k_{bs}(\mathcal{R},\tau)$ (16) yields

$$k_{bs}(\mathcal{R},\tau)=0. \tag{24}$$

http://dx.doi.org/10.5772/56460

Therefore, $v_{bs}(\mathcal{R},\tau)$ depends only on time [see (22)], and in order to define $v_{bs}(\mathcal{R},\tau)$ we can evaluate it at any convenient point, e.g., $\mathcal{R}=1$. The expression for the stress distribution, given by (23), can be simplified by means of [20]

$$E\left[\frac{4x}{(1+x)^2}\right]=(1+x)\left[2E\left(x^2\right)-\left(1-x^2\right)K\left(x^2\right)\right],\quad x\le 1,$$

$$K\left[\frac{4x}{(1+x)^2}\right]=(1+x)\,K\left(x^2\right),\quad x\le 1,$$

such that

$$\Xi_0(\xi,\tau)=-\frac{2}{\pi^{3/2}\tau^{1/2}}\frac{E\left(\xi^2\right)}{1-\xi^2},\quad \xi\le 1. \tag{25}$$

Now, using the integral representation of the elliptic integral

$$E(x)=\int_0^1\sqrt{\frac{1-xt^2}{1-t^2}}dt,$$

one can calculate $v_{bs}(\mathcal{R},\tau)$ [see (17)]

$$v_{bs}(\mathcal{R},\tau)=-\frac{3}{2}\tau^{-1/2}. \tag{26}$$

Large-time asymptotes of $k_{bs}(\mathcal{R},\tau)$ and $v_{bs}(\mathcal{R},\tau)$

The large-time asymptote of $\Xi(\xi,\tau)$ is given by [15]

$$\Xi_\infty(\xi,\tau)=-\tilde{\Pi}_\infty^{(0)}(\xi)\left[\delta(\tau)-2(\pi\tau)^{-3/2}\right]-\frac{8}{3}(\pi\tau)^{-3/2}, \tag{27}$$

where $\delta(\tau)$ is the Dirac delta function and

$$\tilde{\Pi}_\infty^{(0)}(\xi)=\begin{cases}1, & \xi\le 1\\ \frac{2}{\pi}\arctan\left(\frac{1}{\sqrt{\xi^2-1}}\right), & \xi>1\end{cases}.$$

Note that in the leading order we have separation of variables.

Substitution of this large-time asymptote $\Xi_\infty(\xi,\tau)$ into the definitions of $k_{bs}(\mathcal{R},\tau)$ and $v_{bs}(\mathcal{R},\tau)$, given by (16) and (17), leads to

$$k_{bs}(\mathcal{R},\tau) = -\frac{2\delta(\tau)}{\sqrt{\pi}} + \mathcal{O}\left(\tau^{-3/2}\right), \tag{28}$$

$$v_{bs}(\mathcal{R},\tau) = -\frac{3\mathcal{R}^2-1}{\sqrt{\pi}}\delta(\tau) + \mathcal{O}\left(\tau^{-3/2}\right). \tag{29}$$

5. Asymptotic solutions

Details on the derivation of the asymptotic solutions, corresponding to each of the vertices of the parametric space, can be found in [15]. Here we simply list the solutions for the K_0-, $\tilde{K}_{\kappa 0}$-, and $\tilde{K}_{\sigma 0}$-vertices, as well as for the self-similar $\tilde{K}_{\kappa\infty}\tilde{K}_{\sigma\infty}$-edge. These solutions are actually expressed in the same time-independent scaling that corresponds to $\mathcal{G}_\sigma = 1$. In other words, all the solutions are given in terms of the scaled radius $\rho(\tau)$ function of the dimensionless time τ

$$\rho(\tau) = \frac{R(t)}{L_{\text{tr}}}, \qquad \tau = \frac{t}{T}, \tag{30}$$

where

$$L_{\text{tr}} = \left(\frac{K_{Ic}}{\sigma_0 - p_0}\right)^2, \qquad T = \frac{L_{\text{tr}}^2}{4c}. \tag{31}$$

Besides the asymptotic expressions for $\rho(\tau)$, $K_{bs}(\tau)$, $V_{bs}(\tau)$, $\Pi(\tau)$, we have also provided expressions for the hydraulic fracturing efficiency $\mathcal{E}$, defined as $\mathcal{E} \equiv V_{\text{crack}}/V_{\text{inject}}$.

- K_0-vertex

$$\rho_0(\tau) = \left(\frac{3}{8\sqrt{\pi}G_v}\right)^{2/5}\tau^{2/5}, \qquad K_{bs0}(\tau) = 0,$$

$$V_{bs0}(\tau) = -\frac{3}{2}\eta\frac{\pi^{1/2}\tau^{1/2}}{\rho_0^{1/2}(\tau)}\left[\frac{\Gamma(9/5)}{\Gamma(23/10)} + \frac{\pi^{1/2}}{2\rho_0^{1/2}(\tau)}\frac{\Gamma(8/5)}{\Gamma(21/10)}\right],$$

$$\Pi_0(\tau) = \frac{\pi^{1/2}}{2}\rho_0^{-1/2}(\tau), \qquad \mathcal{E}_0(\tau) = \frac{8\sqrt{\pi}}{3}G_v\frac{\rho_0^{5/2}(\tau)\left[1+V_{bs0}(\tau)\right]}{\tau};$$

- $\tilde{K}_{\kappa 0}$-vertex

$$\rho_\kappa(\tau) = \pi^{-4/3}G_c^{-2/3}\left(1-\frac{\eta G_v}{G_c}\right)^{-2/3}\tau^{1/3}, \qquad K_{bs\kappa}(\tau) = 0,$$

http://dx.doi.org/10.5772/56460

$$V_{bs\kappa}(\tau) = -\frac{3}{2}\eta\frac{\pi^{1/2}\tau^{1/2}}{\rho_\kappa^{1/2}(\tau)}\left[\frac{\Gamma(5/3)}{\Gamma(13/6)} + \frac{\pi}{4\rho_\kappa^{1/2}(\tau)}\right],$$

$$\Pi_\kappa(\tau) = \frac{\pi^{1/2}}{2}\rho_\kappa^{-1/2}(\tau), \qquad \mathcal{E}_\kappa(\tau) = \frac{8\sqrt{\pi}}{3}G_v\frac{\rho_\kappa^{5/2}(\tau)\left[1+V_{bs\kappa}(\tau)\right]}{\tau};$$

- $\tilde{K}_{\sigma 0}$-vertex

$$\rho_\sigma(\tau) = 2^{-1/2}\pi^{-3/4}G_c^{-1/2}\left(1-\frac{\eta G_v}{G_c}\right)^{-1/2}\tau^{1/4}, \qquad K_{bs\sigma}(\tau) = 0,$$

$$V_{bs\sigma}(\tau) = -\frac{3}{4}\eta\frac{\pi\tau^{1/2}}{\rho_\sigma^{1/2}(\tau)}\left[1+\frac{1}{\rho_\sigma^{1/2}(\tau)}\frac{\Gamma(11/8)}{\Gamma(15/8)}\right],$$

$$\Pi_\sigma(\tau) = \frac{\pi^{1/2}}{2}\rho_\sigma^{-1/2}(\tau), \qquad \mathcal{E}_\sigma(\tau) = \frac{8\sqrt{\pi}}{3}G_v\frac{\rho_\sigma^{5/2}(\tau)\left[1+V_{bs\sigma}(\tau)\right]}{\tau};$$

- $\tilde{K}_{\kappa\infty}\tilde{K}_{\sigma\infty}$-edge

$$\rho_\infty(\tau) = \left[\frac{\sqrt{\pi+2(1-\eta)/G_c}-\sqrt{\pi}}{4}\right]^2, \qquad \Pi_\infty(\tau) = \frac{\pi^{1/2}}{2}\frac{\rho_\infty^{-1/2}(\tau)}{1-\eta}+\frac{\eta}{1-\eta},$$

$$V_{bs\infty}(\tau) = K_{bs\infty}(\tau) = -\frac{2}{\sqrt{\pi}}\eta\rho_\infty^{1/2}(\tau)\left[1+\Pi_\infty(\tau)\right], \quad \mathcal{E}_\infty(\tau) = \frac{8\sqrt{\pi}}{3}G_v\frac{\rho_\infty^{5/2}(\tau)}{\tau}.$$

6. Transient solution

To obtain a general trajectory of the system starting at the K_0-vertex and ending at the $\tilde{K}_{\kappa\infty}\tilde{K}_{\sigma\infty}$-edge, an implicit numerical algorithm to solve the set of governing equations (12)-(17) has been developed [15].

The results of the numerical simulations for different values of the parameters G_i are presented in Figs 4-7. Depending on the values of the parameters G_i, the system can travel through different vertices, although the journey always has to start at the K_0-vertex and terminate on the $\tilde{K}_{\kappa\infty}\tilde{K}_{\sigma\infty}$-edge.

In some cases the propagation of the fracture terminates before it arrives to the $\tilde{K}_{\kappa\infty}\tilde{K}_{\sigma\infty}$-edge (see Figs 6-7). In these cases, the system, going through a diffusion-dominated vertices, arrives to a point when the dilation of the poroelastic medium $\sim V_{bs}$ is very large, such that

the volume of the fracture becomes equal to zero. The fracture closure time can easily be estimated by substituting the above analytical expressions for V_{bs} and K_{bs} into $V_{\text{crack}}(\tau) \sim 1 + V_{bs}(\tau) - K_{bs}(\tau) = 0$, and solving it with respect to time τ. Note that this estimate is based only on the total volume of fracture and does not address the issue as to when and where the two faces of the fracture first become into contact. In fact, the fracture will first evolve towards a viscosity-dominated propagation regime then close. In other words, a decrease of fracture opening leads to an increase of the pressure gradient of the viscous fracturing fluid, which in turn leads to an increase of the viscous dissipation and eventually to the violation of the zero viscosity assumption for the fracturing fluid. Moreover the fluid pressure profile inside the fracture becomes to be strongly nonuniform, and thus one cannot use the results of the auxiliary problem to model the poroelastic effects. More sophisticated models are needed to study this situation.

7. Discussion

Let us consider the results from an application point of view. Table 2 list the parameters for a re-injection of production water [21]. The values for S and c were estimated on the assumption that $K_{\text{f}}/E \ll 1$ [22].

To characterize the propagation of a fracture, the transition times were calculated using the expressions found in Section 3, see Table 3. In this example, all time scales are well separated. As a result, the fracture follows the edges with the shortest transition time starting at the K_0-vertex, passing through the $\tilde{K}_{\sigma 0}$-vertex, and ending up at the $\tilde{K}_{\sigma\infty}$-vertex. Moreover the transition time from the K_0-vertex into the $\tilde{K}_{\sigma\infty}$-vertex is very small compared to the treatment time. This means that the treatment design can be based on a constant radius model. This analysis relies only on general results of the scaling analysis and does not involve any explicit asymptotic solutions.

	low porosity reservoir (LPR)	**mean porosity reservoir (MPR)**
porosity ϕ (%)	10	20
permeability k (md)	10	100
Young's modulus E (GPa)	30	15
Poisson's ratio ν	0.2	0.25
rock toughness K_{Ic} (MPa $\cdot$ m$^{1/2}$)	1.0	
water bulk modulus K_{f} (GPa)	2.2	
water viscosity μ (mPa $\cdot$ s)	1.0	
Biot coefficient α	0.6	
diffusion coefficient c (m^2/s)	0.212	1.04
storage coefficient S (Pa^{-1})	4.65×10^{-11}	9.49×10^{-11}
poroelastic stress modulus η	0.225	0.2
reservoir thickness H (m)	50	5
confining stress σ_0 (MPa)	55	
initial pore pressure p_0 (MPa)	30	
injection rate Q_0 (m^3/day)	750	
treatment time T (days)	100	

Table 2. Characteristic parameters during production water re-injection [21]

http://dx.doi.org/10.5772/56460

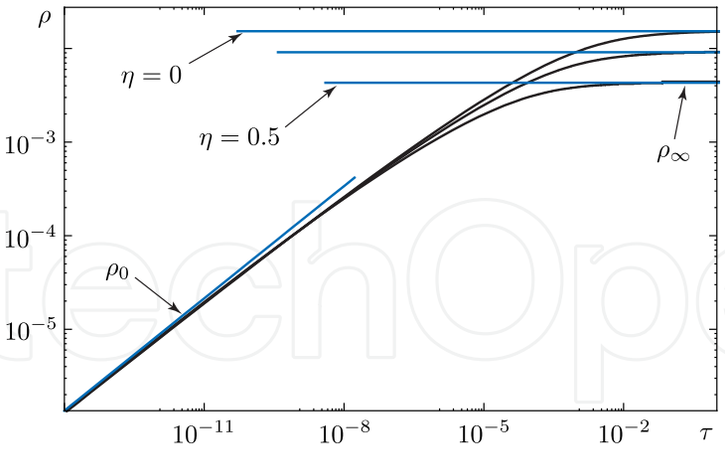

(a) Fracture radius ρ vs time τ

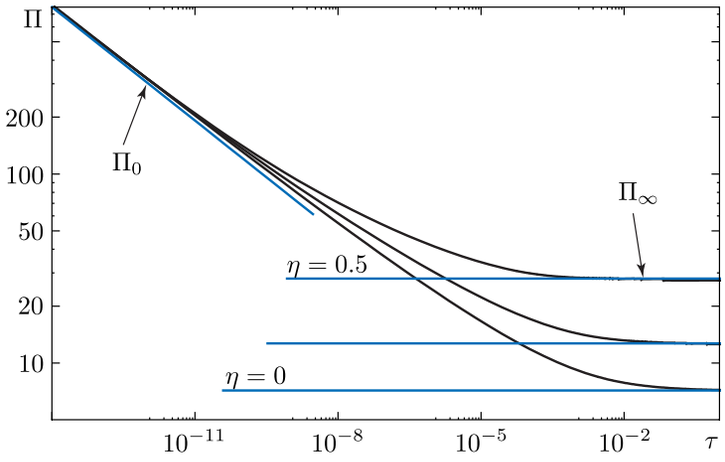

(b) Fracturing fluid pressure Π vs time τ

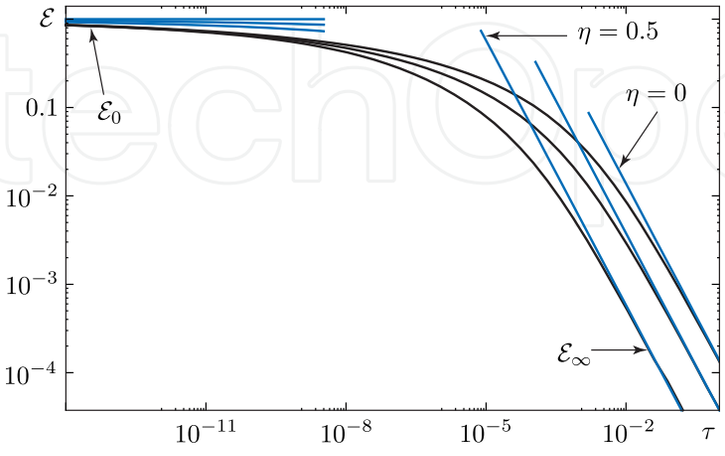

(c) Hydraulic fracturing efficiency $\mathcal{E}$ vs time τ

Figure 4. General case $G_v = G_c = 1$, $\eta = 0.0, 0.25, 0.5$

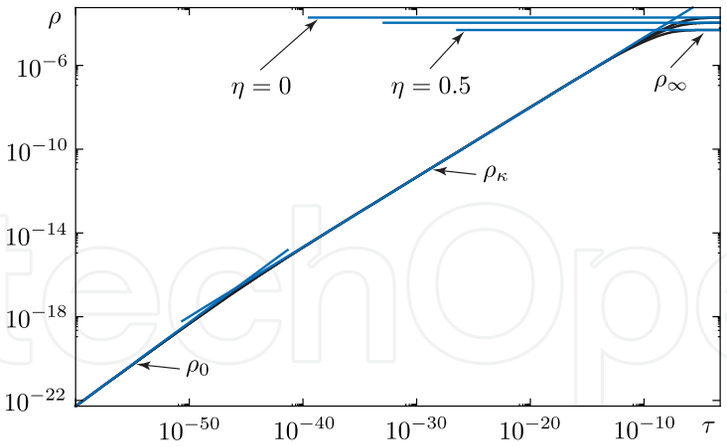

(a) Fracture radius ρ vs time τ

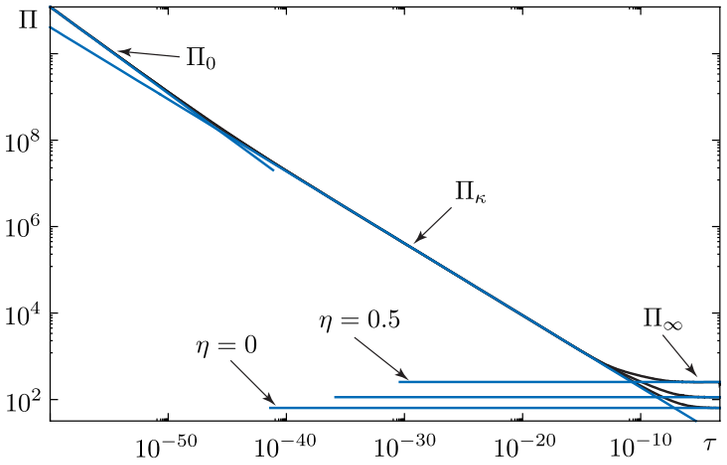

(b) Fracturing fluid pressure Π vs time τ

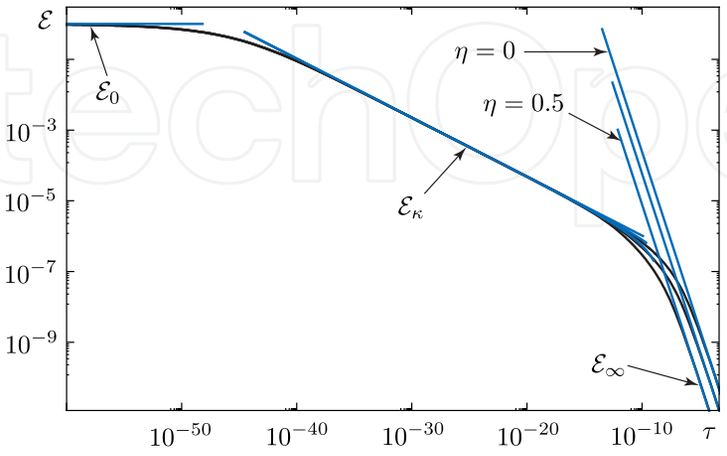

(c) Hydraulic fracturing efficiency $\mathcal{E}$ vs time τ

Figure 5. Case $G_v = 10^{-5}$, $G_c = 10$, $\eta = 0.0, 0.25, 0.5$. Here the fracture goes through the $\tilde{K}_{\kappa 0}$-vertex

http://dx.doi.org/10.5772/56460

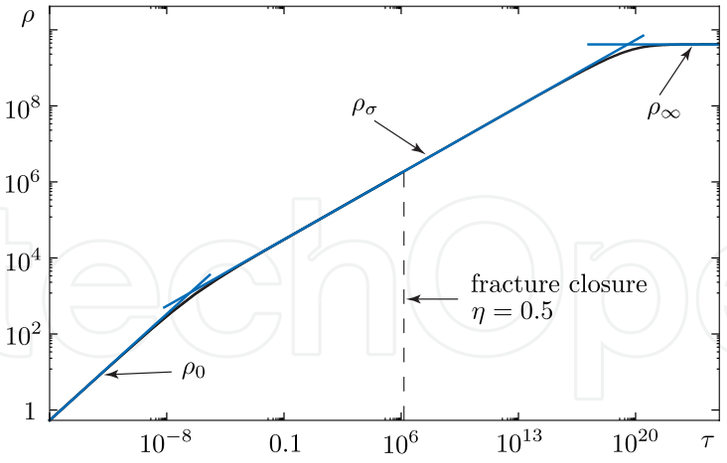

(a) Fracture radius ρ vs time τ

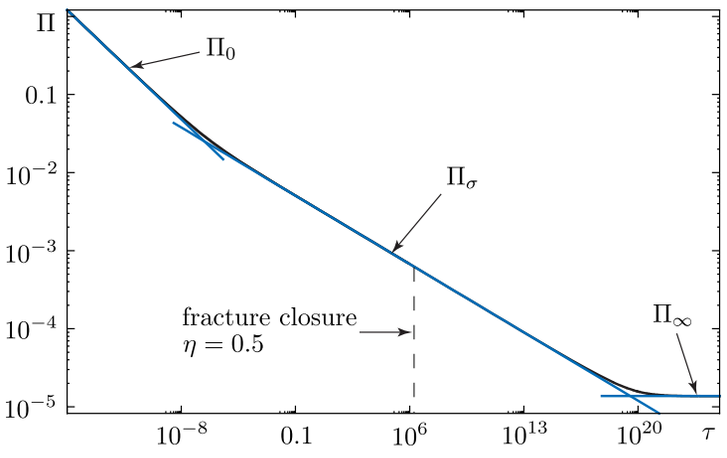

(b) Fracturing fluid pressure Π vs time τ

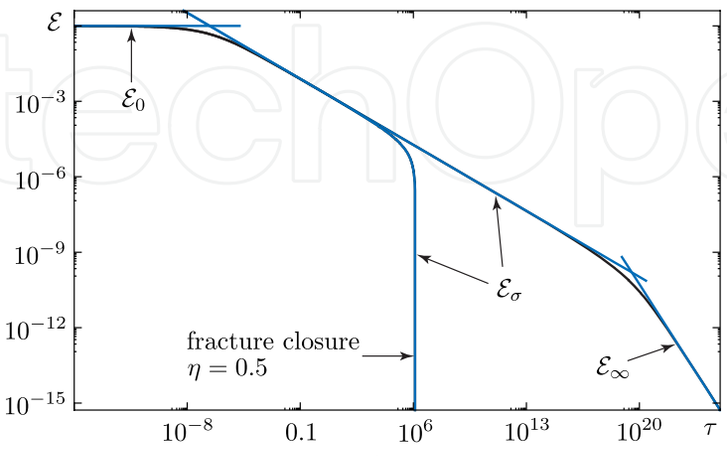

(c) Hydraulic fracturing efficiency $\mathcal{E}$ vs time τ

Figure 6. Case $G_v = 10^{-15}$, $G_c = 3 \times 10^{-11}$, $\eta = 0.0, 0.5$. Here the fracture goes through the $\tilde{K}_{\sigma 0}$-vertex

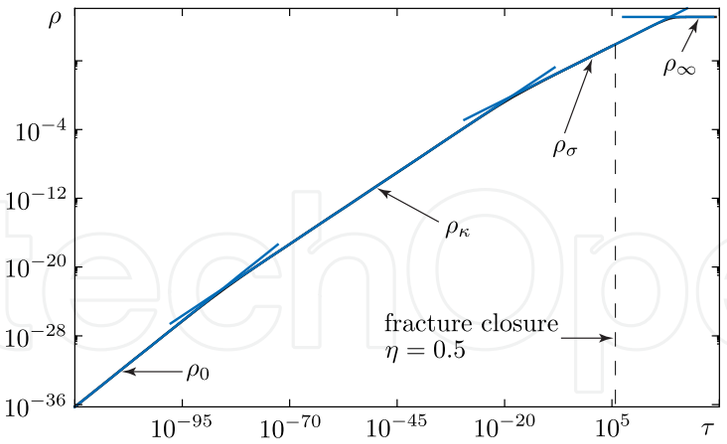

(a) Fracture radius ρ vs time τ

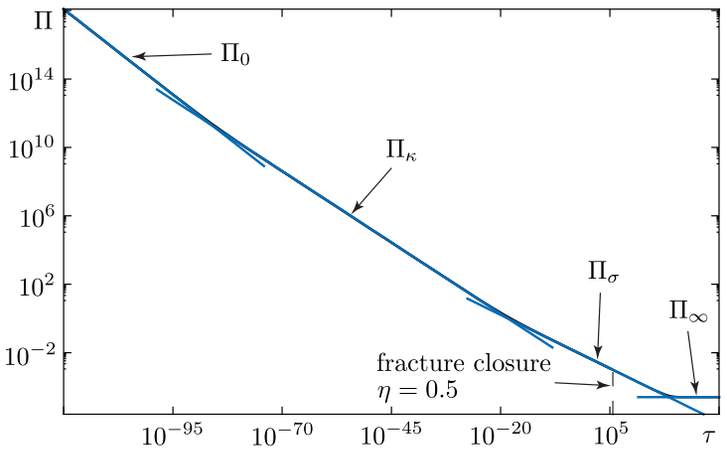

(b) Fracturing fluid pressure Π vs time τ

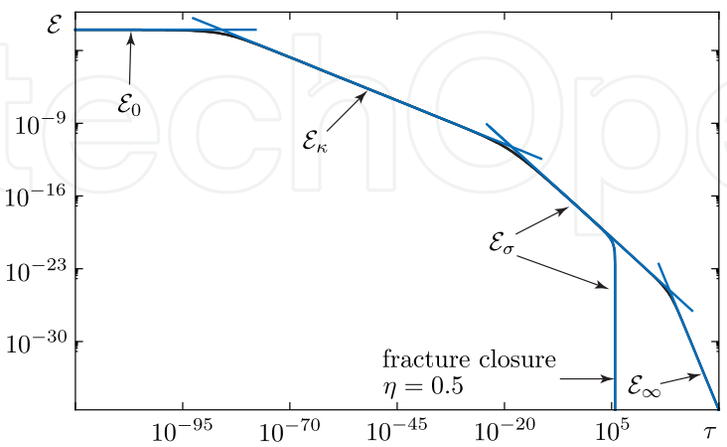

(c) Hydraulic fracturing efficiency $\mathcal{E}$ vs time τ

Figure 7. Case $G_c = 10^{-10}$, $\eta = 0.0, 0.5$. Here the fracture goes through the $\tilde{K}_{\kappa 0}$- and $\tilde{K}_{\sigma 0}$-vertices

http://dx.doi.org/10.5772/56460

current vertex	possible transitions: vertex	transition time: LPR, sec	transition time: MPR, sec	vertex choice
K_0	K_∞	1.2×10^{13}	3.1×10^{8}	
	$\tilde{K}_{\kappa 0}$	4.6×10^{16}	8.3×10^{9}	
	$\tilde{K}_{\sigma 0}$	0.087	1.7×10^{-3}	$\tilde{K}_{\sigma 0}$
$\tilde{K}_{\sigma 0}$	$\tilde{K}_{\sigma\infty}$	5.8×10^{3}	11.9	$\tilde{K}_{\sigma\infty}$

Table 3. Crack propagation

At the $\tilde{K}_{\sigma\infty}$-vertex the fracture radius is equal to $R \approx 3.4$ m and the net pressure is $p - \sigma_0 \approx 7.4$ MPa in the LPR case, whereas $R \approx 0.35$ m and $p - \sigma_0 \approx 7.2$ MPa for the MPR case. If one does not take into account the poroelastic effect, the fracture would grow to $R \approx 4.4$ m and $p - \sigma_0 \approx 0.071$ MPa in the LPR case, while $R \approx 0.44$ m and $p - \sigma_0 \approx 0.71$ MPa in the MPR case. Thus the ultimate fracture radius decrease due to the poroelastic effects is not so significant. On the other hand, the net pressure increase is significant (about 100- and 10-fold increase in the LPR and MPR case, respectively).

In the above analysis we have assumed that the fracture propagates in the toughness-dominated regime (fracturing fluid of zero viscosity). To check this assumption, the value of the following dimensionless group (known as the dimensionless viscosity [17]) has to be assessed

$$\mathcal{G}_m(t) = \frac{\mu' Q_0 E'^3}{K_{Ic}^4 L(t)}, \tag{32}$$

where $L(t)$ is the characteristic fracture size. If the fracture propagates in a viscosity-dominated regime, then $\mathcal{G}_m(t) \gg 1$. In the toughness-dominated regime, $\mathcal{G}_m(t) \ll 1$. Using the above data one can find that at the $\tilde{K}_{\sigma\infty}$-vertex this dimensionless group is equal to $\mathcal{G}_m \approx 90$ for the LPR and $\mathcal{G}_m \approx 121$ for the MPR. Thus fracturing fluid viscosity should be taken into account. Nevertheless, the above example illustrates the importance of the poroelastic effects. In fact a rigorous analysis of the viscosity-dominated regimes predicts similar values for the fracture size and the net pressure [15].

The numerical simulations reported in Figs 4-7 sweep huge time ranges. This is a consequence of the small-time asymptote (K_0-vertex) as the initial condition combined with the need to start from a physically correct initial condition to construct accurate numerical solutions. In practice, however, a correct assessment of the relevant part of the parametric space can dramatically simplify the situation. Knowing this information one can use the analytical vertex asymptotes for preliminary estimation, and then optimize a numerical algorithm. For example Figs 5-7 illustrate that one can use the asymptotic solution of an intermediate vertex as the initial condition provided that the transition time from the K_0-vertex into this vertex is small compared to the treatment time. In the above example of production water reinjection, we have shown that the fracture propagation arrests within a very short period of time compared to the characteristic treatment time. Thus from a practical point of view in this case one can simply use the analytical large-time asymptote to design the treatment.

8. Conclusions

This paper has described a detailed study of a penny-shaped fracture driven by a zero viscosity fluid through a poroelastic medium. The main contribution of this study is the consideration of large scale 3D diffusion and the related poroelastic effect (backstress). We have shown that the problem under consideration has six self-similar propagation regimes (see Section 3). In particular we have demonstrated the existence of a regime ($\tilde{K}_{\kappa\infty}\tilde{K}_{\sigma\infty}$-edge) where the fracture stops propagating. In this regime the fracturing fluid injection is balanced by the 3D fluid leak-off. This stationary solution in the case of zero backstress, $\eta = 0$, was originally obtained by [13].

Numerical simulations illustrate that poroelastic effects could have a significant influence on the propagation of a hydraulic fracture. Namely in the case of 3D diffusion, the backstress effect leads to a decrease of the fracture radius (see Figs 4a and 5a) accompanied by an increase of the fracturing fluid pressure (see Figs 4b and 5b). Moreover, the poroelastic effects can lead to premature closure of a fracture propagating in a leak-off dominating regime with 1D diffusion.

The technique developed in this paper could be also applied to the problem of in situ stress determination by hydraulic fracture [23]. In this application the *in situ* stress determination relies on the interpretation of the fracture breakdown and reopening fluid pressure as well as of the fracture closure pressure during the shut-in phase of experiment. It is obvious that the poroelastic effects could lead to a significant corrections into the stress measurements.

Author details

Yevhen Kovalyshen[1,⋆] and Emmanuel Detournay[1,2]

⋆ Address all correspondence to: Yevhen.Kovalyshen@csiro.au

1 Drilling Mechanics Group, CSIRO Earth Science and Resource Engineering, Australia
2 Department of Civil Engineering, University of Minnesota, USA

References

[1] D.A. Mendelsohn. A review of hydraulic fracture modeling - part i: General concepts, 2d models, motivation for 3d modeling. *jert*, 106:369–376, 1984.

[2] M.J. Economides and K.G. Nolte, editors. *Reservoir Stimulation*. John Wiley & Sons, Chichester UK, 3rd edition, 2000.

[3] A.S. Abou-Sayed. Safe injection pressures for disposing of liquid wastes: a case study for deep well injection (SPE/ISRM-28236). In Balkema, editor, *Proceedings of the Second SPE/ISRM Rock Mechanics in Petroleum Engineering*, pages 769–776, 1994.

[4] J. Hagoort, B. D. Weatherill, and A. Settari. Modeling the propagation of waterflood-induced hydraulic fractures. *Soc. Pet. Eng. J.*, pages 293–301, August 1980.

[5] M. Blunt, F.J. Fayers, and F.M. Orr. Carbon dioxide in enhanced oil recovery. *Energy Convers. Mgmt*, 34(9-11):1197–1204, 1993.

[6] A. van As and R.G. Jeffrey. Caving induced by hydraulic fracturing at Northparkes mines. In *Pacific Rocks 2000*, pages 353–360, Rotterdam, 2000. Balkema.

[7] R.G. Jeffrey and K.W. Mills. Hydraulic fracturing applied to inducing longwall coal mine goaf falls. In *Pacific Rocks 2000*, pages 423–430, Rotterdam, 2000. Balkema.

[8] J. Adachi, E . Siebrits, A. P. Peirce, and J. Desroches. Computer simulation of hydraulic fractures. *Int. J. Rock Mech. Min. Sci.*, 44(5):739–757, International Journal of Rock Mechanics and Mining Sciences 2007.

[9] E.D. Carter. Optimum fluid characteristics for fracture extension. In G.C. Howard and C.R. Fast, editors, *Drilling and Production Practices*, pages 261–270. American Petroleum Institute, Tulsa OK, 1957.

[10] M. P. Cleary. Analysis of mechanisms and procedures for producing favourable shapes of hydraulic fractures. In *Proc. 55th Annual Fall Technical Conference and Exhibition of the Society of Petroleum Engineers of AIME*, volume SPE 9260, pages 1–16, September 1980.

[11] E. Detournay and A.H-D. Cheng. Plane strain analysis of a stationary hydraulic fracture in a poroelastic medium. *Int. J. Solids Structures*, 27(13):1645–1662, 1991.

[12] A.P. Bunger, E. Detournay, and D.I. Garagash. Toughness-dominated hydraulic fracture with leak-off. *Int. J. Fracture*, 134(2):175–190, 2005.

[13] S. A. Mathias and M. Reeuwijk. Hydraulic fracture propagation with 3-d leak-off. *Transport in Porous Media*, 2009.

[14] I. Berchenko, E. Detournay, and N. Chandler. Propagation of natural hydraulic fractures. *Int. J. Rock Mech. Min. Sci.*, 34(3-4), 1997.

[15] Y. Kovalyshen. *Fluid-Driven Fracture in Poroelastic Medium*. PhD thesis, University of Minnesota, Minneapolis, February 2010.

[16] D.T. Barr. *Leading-Edge Analysis for Correct Simulation of Interface Separation and Hydraulic Fracturing*. PhD thesis, Massachusetts Institute of Technology, Cambridge MA, 1991.

[17] A.A. Savitski and E. Detournay. Propagation of a fluid-driven penny-shaped fracture in an impermeable rock: Asymptotic solutions. *Int. J. Solids Structures*, 39(26):6311–6337, 2002.

[18] M. Abramowitz and I.A. Stegun, editors. *Handbook of Mathematical Functions with Formulas, Graphs, and Mathematical Tables*. Dover Publications Inc., New York NY, 1972.

[19] E. Detournay. Propagation regimes of fluid-driven fractures in impermeable rocks. *Int. J. Geomechanics*, 4(1):1–11, 2004.

[20] I.S. Gradshteyn and I.M. Ryzhik. *Table of Integrals, Series and Products*. Academic Press, San Diego CA, 5th edition, 1994.

[21] P. Longuemare, J-L. Detienne, P. Lemonnier, M. Bouteca, and A. Onaisi. Numerical modeling of fracture propagation induced by water injection/re-injection. *SPE European Formation Damage, The Hague, The Netherlands*, May 2001. (SPE 68974).

[22] E. Detournay and A.H-D. Cheng. *Comprehensive Rock Engineering*, volume 2, chapter 5: Fundamentals of Poroelasticity, pages 113–171. Pergamon, New York NY, 1993.

[23] E. Detournay, A. H-D Cheng, J. C. Roegiers, and J. D. Mclennan. Poroelasticity considerations in in situ stress determination by hydraulic fracturing. *Int. J. Rock Mech. Min. Sci.*, 26(6):507–513, 1989.